

# Multi-mission observations of the old nova GK Per during the 2015 outburst

P. Zemko<sup>1\*</sup>, M. Orío<sup>2,3</sup>, G. J. M. Luna<sup>4,5</sup>, K. Mukai<sup>6,7</sup>, P. A. Evans<sup>8</sup>, and A. Bianchini<sup>1,2</sup>

<sup>1</sup>*Department of Physics and Astronomy, Università di Padova, vicolo dell' Osservatorio 3, I-35122 Padova, Italy*

<sup>2</sup>*INAF - Osservatorio di Padova, vicolo dell' Osservatorio 5, I-35122 Padova, Italy*

<sup>3</sup>*Department of Astronomy, University of Wisconsin, 475 N. Charter Str., Madison, WI 53704, USA*

<sup>4</sup>*Universidad de Buenos Aires, Facultad de Ciencias Exactas y Naturales, Av. Inte. Güiraldes 2620, C1428ZAA, Buenos Aires, Argentina*

<sup>5</sup>*CONICET-Universidad de Buenos Aires, Instituto de Astronomía y Física del Espacio, (IAFE), Av. Inte. Güiraldes 2620, C1428ZAA, Buenos Aires, Argentina*

<sup>6</sup>*CRESST and X-ray Astrophysics Laboratory, NASA Goddard Space Flight Center, Greenbelt, MD 20771, USA*

<sup>7</sup>*Department of Physics, University of Maryland, Baltimore County, 1000 Hilltop Circle, Baltimore, MD 21250, USA*

<sup>8</sup>*Department of Physics and Astronomy, University of Leicester, Leicester LE1 7RH, UK*

## ABSTRACT

GK Per, a classical nova of 1901, is thought to undergo variable mass accretion on to a magnetized white dwarf (WD) in an intermediate polar system (IP). We organized a multi-mission observational campaign in the X-ray and ultraviolet (UV) energy ranges during its dwarf nova (DN) outburst in 2015 March–April. Comparing data from quiescence and near outburst, we have found that the maximum plasma temperature decreased from about 26 to  $16.2^{+0.5}_{-0.4}$  keV. This is consistent with the previously proposed scenario of increase in mass accretion rate while the inner radius of the magnetically disrupted accretion disc shrinks, thereby lowering the shock temperature. A *NuSTAR* observation also revealed a high-amplitude WD spin modulation of the very hard X-rays with a single-peaked profile, suggesting an obscuration of the lower accretion pole and an extended shock region on the WD surface. The X-ray spectrum of GK Per measured with the *Swift* X-Ray Telescope varied on time-scales of days and also showed a gradual increase of the soft X-ray flux below 2 keV, accompanied by a decrease of the hard flux above 2 keV. In the *Chandra* observation with the High Energy Transmission Gratings, we detected prominent emission lines, especially of Ne, Mg and Si, where the ratios of H-like to He-like transition for each element indicate a much lower temperature than the underlying continuum. We suggest that the X-ray emission in the 0.8–2 keV range originates from the magnetospheric boundary.

**Key words:** (stars:) novae, cataclysmic variables — stars: individual: GK Per

## 1 INTRODUCTION

GK Per underwent a nova explosion on 1901 February 21 (Williams 1901) and after a long period of irregular fluctuations, in 1948, it started to behave like a dwarf nova (DN), with small amplitude (1–3 mag.) outbursts lasting for up to two months and recurring at intervals that can be roughly expressed as  $n \times (400 \pm 40)$  days (Sabbadin & Bianchini 1983). The widely accepted explanation of these outbursts is a recurring thermal instability in the inner part of the accretion disc (inside-out outbursts; see Bianchini et al. 1986,

Kim et al. 1992 for the application of the disc instability model to GK Per).

GK Per, at a distance of 470 pc (McLaughlin 1960), is the second closest nova to us and the best monitored at quiescence. It is surrounded by an expanding nova shell, which emits in the X-rays (Balman 2005; Takei et al. 2015), weakly in UV (Evans et al. 1992), optical (e.g. Shara et al. 2012), infrared (e.g. Eyres et al. 1999) and radio (Anupama & Kantharia 2005) bands and has a complex structure with numerous knots (Liimets et al. 2012) and a jet-like feature.

The orbital period is 1.9968 d (Crampton et al. 1986; Morales-Rueda et al. 2002). The secondary is a K2-type subgiant mass of 0.25–0.48  $M_{\odot}$  (Warner 1976; Watson et al.

\* E-mail: polina.zemko@studenti.unipd.it

1985; Morales-Rueda et al. 2002) and the mass of the primary is  $0.86 \pm 0.02 M_{\odot}$  (Suleimanov et al. 2016). GK Per has an extended accretion disc ( $\sim 10^{11}$  cm) and interpreting the typical duration of DN outbursts in GK Per as the viscous decay time-scale Evans et al. (2009b) find that only about 10 % of the disc is involved in the outbursts.

King et al. (1979) and Bianchini & Sabadin (1983) proposed that GK Per hosts a magnetic white dwarf (WD). Watson et al. (1985) discovered a modulation with a 351 s period in the X-ray light curve and proposed that this is the WD spin period. Watson et al. (1985) also noticed that the pulse fraction is 50 % above 3 keV and up to 80 % below 3 keV, but does not depend on the mean X-ray flux. The pulse profile is single-peaked in outburst and double-peaked, with smaller amplitude in quiescence (Norton et al. 1988; Hellier et al. 2004).

Apart from the spin-related modulation, during outbursts GK Per shows quasi periodic oscillations (QPOs) in X-rays and in the optical band with the characteristic time-scale of several kiloseconds (e.g. Watson et al. 1985; Morales-Rueda et al. 1999; Nogami et al. 2002; Hellier et al. 2004). This time-scale is exceptionally long compared to what is typically observed in CVs (Warner 2004). QPOs with periods of 360–390 s were also detected in optical observations of GK Per by several authors. Watson et al. (1985) noticed that the beat period between the spin period and the shorter-period QPOs is in the kiloseconds range, close to the period of the longer QPOs. Morales-Rueda et al. (1999) explored this idea, assuming that the QPOs are due to absorption of the emission from the innermost regions of the accretion disc by blobs of material in the magnetosphere. The 360–380 s period in this model is due to the Keplerian velocity in the inner disc radius. Hellier et al. (2004) argued that this scenario explains the optical data of Morales-Rueda et al. (1999), but does not fit the X-ray observations. These authors suggested instead that bulges of material in the inner edge of the accretion disk, high above the disc plane, obscure the WD and the  $\sim 5000$ s period is due to the slow-moving prograde waves in the innermost region of the disc (Warner & Woudt 2002).

Several pieces of evidence indicate that during DN outbursts the accretion disk in GK Per pushes the magnetosphere towards the surface of the WD (Hellier et al. 2004; Vrielmann et al. 2005; Suleimanov et al. 2016) as expected by theory (see, e.g., Ghosh & Lamb 1979). This scenario, first proposed by Hellier et al. (2004) in analogy with XY Ari (Hellier et al. 1997), explains the single-peaked pulse profile as a consequence of cutting off the line of sight to the lower accreting pole. The maximum plasma temperature in GK Per in quiescence is higher than in outburst (Brunschweiler et al. 2009), which can also be understood in the context of the shrinking of the accretion disc (Suleimanov et al. 2005). However, while the hard X-ray emission can be explained as due to the accretion columns emitting bremsstrahlung radiation that is highly absorbed, the broad-band X-ray spectrum of GK Per and its evolution during outbursts are much more complex. Šimon (2015) noticed that the halt of the rise of the hard X-ray luminosity is not modelled only by just assuming increased absorption, and probably involves large structural changes of the accreting regions. Mukai et al. (2003) have shown that the outburst X-ray spectrum of GK Per below 2 keV is not con-

sistent with a “typical” cooling-flow spectrum of an accreting WD and proposed a considerable contribution of photoionization. Vrielmann et al. (2005) and Evans & Hellier (2007) noticed that the soft X-ray emission of GK Per detected during the 2002 outburst may originate in the heated surface of the WD, like in the case of “soft intermediate polars”.

On 2015 March 6.84 Dubovsky (VSNET-ALERT 18388) and Schmeer (VSNET-ALERT 18389) discovered that GK Per has started a new DN outburst and was at a magnitude 12.8. We proposed a multimission observation campaign in order to follow the evolution of the object during the outburst and to obtain X-ray spectra in a broad energy range, revealing the physical processes that take place in this binary system.

## 2 X-RAY OBSERVATIONS AND DATA ANALYSIS

We started the observations of the 2015 DN outburst of GK Per as soon as it became observable with *Swift* on March 12 2015, and we could follow the outburst almost until the optical maximum. We wanted a higher cadence than in the previous 2006 outburst *Swift* monitoring, and obtained two exposures per day for two weeks and one exposure per day in the following two weeks. During the first two weeks of the monitoring the *Swift* X-Ray Telescope (XRT) (Burrows et al. 2005) was in the automatic state (Hill et al. 2005), choosing the photon counting (PC) or window timing (WT) operating mode depending on the source count rate. During the second two weeks the monitoring was performed only in the WT mode. The *Swift* Ultraviolet Optical Telescope (UVOT) was in the image mode, providing the mean magnitude per exposure in one of the four UVOT filters (U, UVW1, UVM2, UVW2). Coordinated *NuSTAR* and *Chandra* Advanced Imaging Spectrometer High-Energy Transmission Grating (ACIS-S/HETG) observations were performed on April 4 2015, close to the optical maximum. The *Chandra* ACIS-S/HETG consists of two sets of gratings (Canizares et al. 2005), operating in the 31–2.5 Å (Medium Energy Grating) and 15–1.2 Å (High Energy Grating) energy ranges with the resolution better than 0.023 Å. *NuSTAR* has two detectors: FPMA and FPMB, covering the same energy range, from 3 to 79 keV. The time resolution of all the instruments used for the observations is better than 2.5 s, which is much shorter than the periodicities we expected to find. The *Swift* XRT spectra and the mean X-ray count rate per snapshot in the 0.3–10 keV energy range were obtained using the *Swift* XRT data products generator (Evans et al. 2009a, 2007), subsequently performing the barycentric correction with an applet<sup>1</sup>, created by Eastman et al. (2010). The *Swift* XRT light curves in the WT mode and in the PC mode (the latter excluding the central region and subsequently running `xrtlccorr`, because of the pile-up) and the UVOT data were processed with the `ftools` package. The *Swift* XRT light curves were barycentric corrected using `barycorr` tool.

We also used the processed *Swift* Burst Allert Telescope (BAT) data from the *Swift* BAT transient monitor

<sup>1</sup> <http://astroutils.astronomy.ohio-state.edu/>

page (Krimm et al. 2013). The *Chandra* data were reduced with CIAO v.4.7 and the *NuSTAR* data with the standard `nuproducts` pipeline. The *NuSTAR* and *Chandra* light curves were barycentric corrected. The X-ray spectra were analysed and fitted with XSPEC v. 12.8.2. The list of the observations with the exposure times and count rates is presented in table 1.

### 3 DEVELOPMENT OF THE OUTBURST

Figure 1 shows a comparison between the development of the outburst in the optical, UV and X-rays. The top panel is the optical light curve, which was obtained from The American Association of Variable Star Observers (AAVSO)<sup>2</sup>. The beginning of the outburst in the optical band was taken as a reference and is marked with the red dashed vertical line in all the panels. The maximum of the outburst in the optical band is also marked with the blue line. The second panel shows the *Swift* UVOT data in different filters. All the UVOT light curves showed a gradual rise. The images in the lower energy filter — U — and the last observations in the UVW1 and UVW2 filters were saturated and provide only lower limits for the magnitudes. We analysed also quiescence *Swift* UVOT observations of GK Per obtained in 2012 to find the amplitude of the outburst in the UV range. Table 2 shows the quiescent UVOT magnitudes.

The third panel is the *Swift* XRT light curve averaged within a snapshot in the whole energy range: from 0.3 to 10 keV. The count rate varied from 0.7 to about 3 cts s<sup>-1</sup> but did not show any significant increasing or decreasing trend.

We missed the initial steep rise, observed only with the *Swift* BAT, because GK Per was too close to the Sun, and observed only a plateau in the *Swift* XRT light curve. In fig. 1, the bottom panels show the soft (0.3–2.0 keV) and hard (2.0–10 keV) XRT light curves. The hard count rate is more scattered in comparison with the soft one and decreased as the outburst developed. The soft count rate, in turn, showed a prominent rise, which resulted in a gradual decrease of the hardness ratio (panel 5) with minimum around MJD 57113, 25 days after the beginning of the outburst. The light curve measured with the *Swift* BAT is more stable and only showed a moderate decrease after maximum around day 10 after the outburst. The flux increase started 2 days earlier in the *Swift* BAT energy range than in optical.

## 4 TIMING ANALYSIS

### 4.1 Broad band power spectra.

For our timing analysis we extracted the *Swift* XRT, *NuSTAR* (the FPMA and FPMB detectors were combined) and *Chandra* light curves and binned them every 10 s. In order to investigate a possible energy dependence of the X-ray variability we split the *Swift* XRT light curve in two ranges: 0.3–2.0 and 2.0–10 keV, the *Chandra* HETG light curve was extracted below 6 Å and above 6 Å and the *NuSTAR* one above and below 10 keV. *Chandra* hard and *NuSTAR* data show a strong periodic modulation, which can be seen in fig.

2. For visibility in fig. 2 the *Chandra* count rate was multiplied by a factor of 20. To study this modulation quantitatively, we constructed Lomb-Scargle periodograms (Scargle 1982) of various data in soft and hard energy bands. The Lomb-Scargle periodograms (LSPs) in a broad range of periods for all the light curves are presented in fig. 3. The top-left-hand panel shows the LSPs of hard (black) and soft (red) *Swift* XRT light curves. The highest peak of the hard LSP corresponds to the WD spin period — 351.33 s. The spin modulation is not present in the LSP of the soft *Swift* XRT light curve: it shows peaks only at longer time scales with the strongest one at 5736 s. Although QPOs in GK Per on a time-scale of ~5000 were reported by many authors, this period is too close to the *Swift* orbital period of 5754 s to be distinguished from the windowing in the observations. The top-right- and bottom-left-hand panels of fig. 3 show the LSPs of the *Chandra* HETG and the *NuSTAR* light curves, respectively. There is no peak in the *Chandra* soft LSP at 5736 s period, which confirms that this peak in the soft *Swift* periodogram does not correspond to a real modulation. On the other hand, the *NuSTAR* and the hard *Chandra* LSPs show peaks at ~7000 s. These light curves are indeed variable on the time-scales of kiloseconds, as shown by fig. 2.

The blue dashed lines in the top-right- and bottom-left-hand panels show the LSPs after the subtraction of the peak corresponding to the spin period. We fitted and subtracted a sine function with a fixed period of 351.33 s from the original data, and plotted the LSPs again. The peak close to half of the spin period remained in the hard *NuSTAR* and *Chandra* LSPs.

### 4.2 Energy dependence of the WD spin modulation.

All the LSPs of the light curves extracted above 2 keV show a prominent peak corresponding to the WD spin period, while neither *Chandra* nor *Swift* soft LSPs show any. The absence of the spin modulation in the region of 0.3 – 2 keV may indicate that this emission component has a different origin and is visible during the whole spin cycle. We also extracted the light curves from the *Chandra* HETG data in the regions of the strongest emission lines of Mg, Si and Fe K $\alpha$  6.4 keV and checked whether the flux in these lines is modulated with the orbital or with the spin period. Only the Fe K $\alpha$  line emission showed spin modulation, while the flux in the other emission lines had aperiodic fluctuations.

The peak corresponding to the spin period is present even in the LSP of the *NuSTAR* light curve above 10 keV. Typically the spin modulation of IPs is not detected, or only marginally measurable, in the hard X-rays (Norton & Watson 1989; Mukai et al. 2015), since the cross-section of the photoelectric absorption that usually causes the modulation decreases with energy. The effect of photoelectric absorption is not significant above 10 keV, so the observed high energy modulation might originate in a different mechanism than absorption of the accretion column emission. The comparison of the phase folded *NuSTAR* light curves in two energy ranges (fig. 3) confirms that the spin modulation is not energy dependent: the spin profiles are almost identical.

<sup>2</sup> <https://www.aavso.org/>

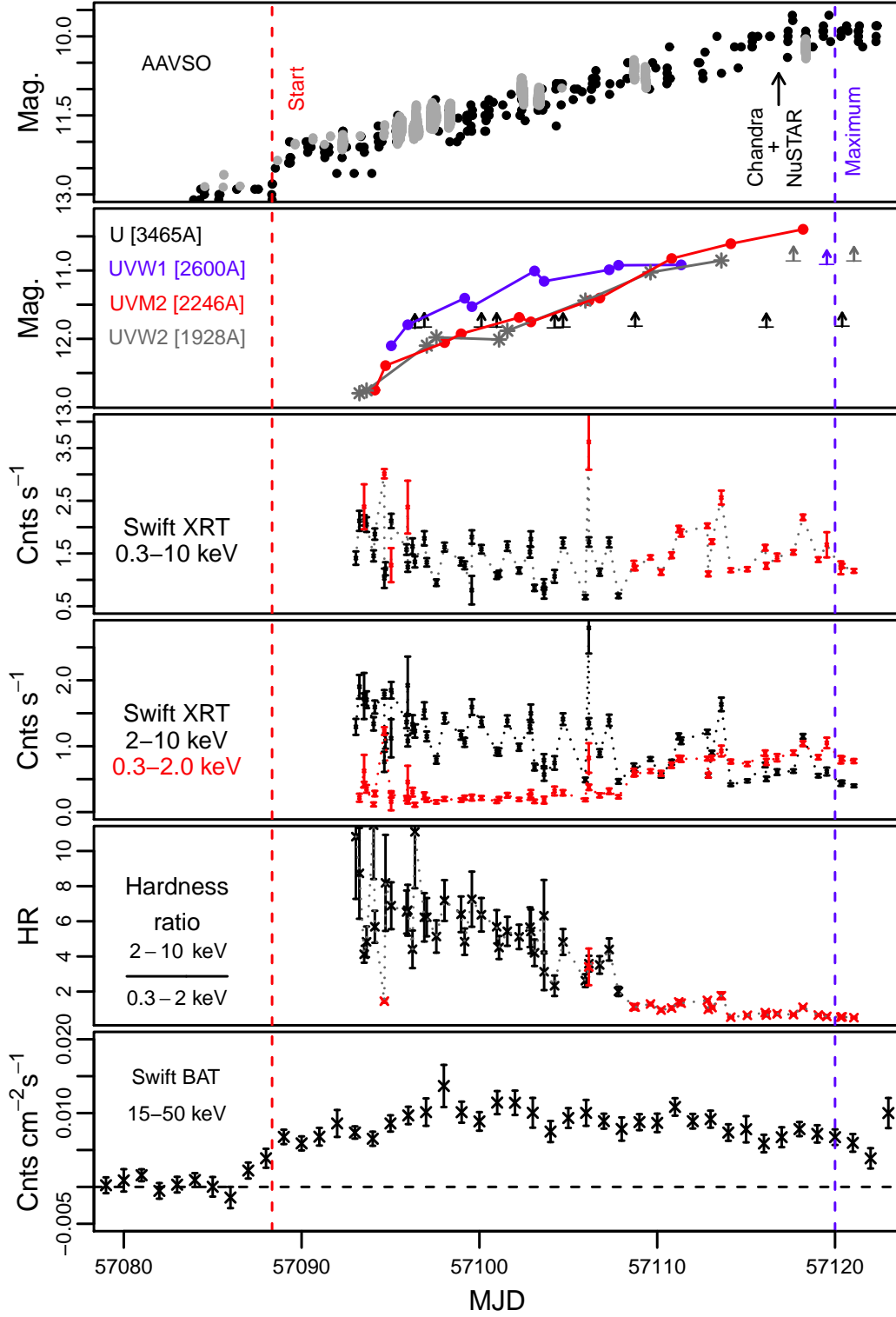


**Figure 1.** From top to bottom: AAVSO light curve in the *V* band (grey) and without a filter (black). The red and blue vertical lines in all the panels mark the beginning (MJD 57088.34) and the maximum (MJD 57120) of the outburst in the optical band. The *Swift* UVOT light curves in different filters. The *Swift* XRT light curve in the PC (red) and WT (black) modes. The *Swift* XRT light curves above 2 keV (black) and below 2 keV (red). The X-ray hardness ratio from the data obtained in the WT (red) and PC (black) modes. The *Swift* BAT light curve.

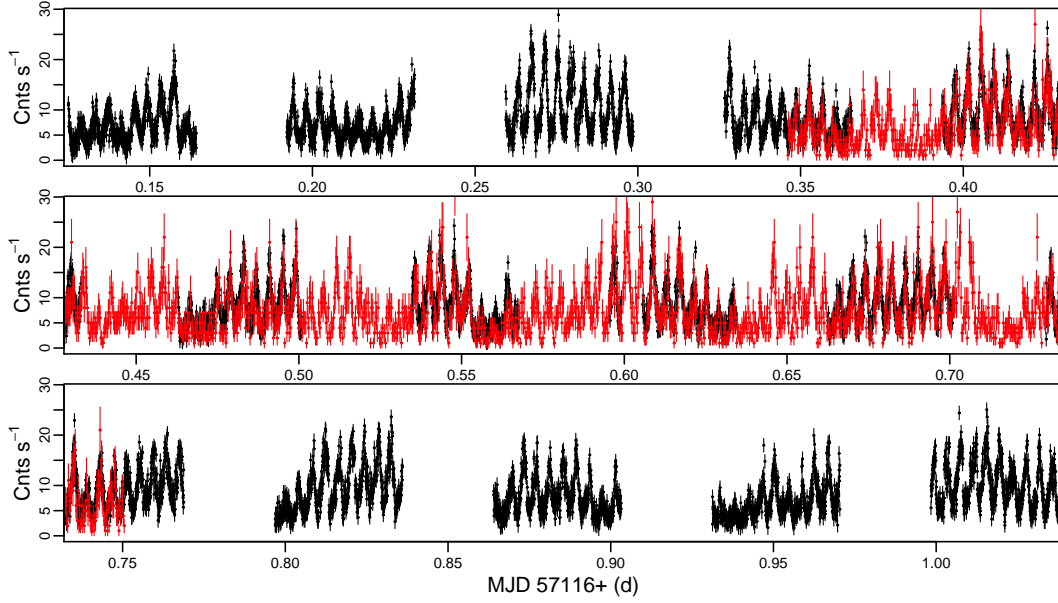


**Figure 2.** *NuSTAR* FPMA+FPMB light curve binned every 10 s (black) and the *Chandra* HETG light curve in the 1–6 Å wavelength range, binned every 20 s (red) and multiplied by a factor of 20 for visibility.

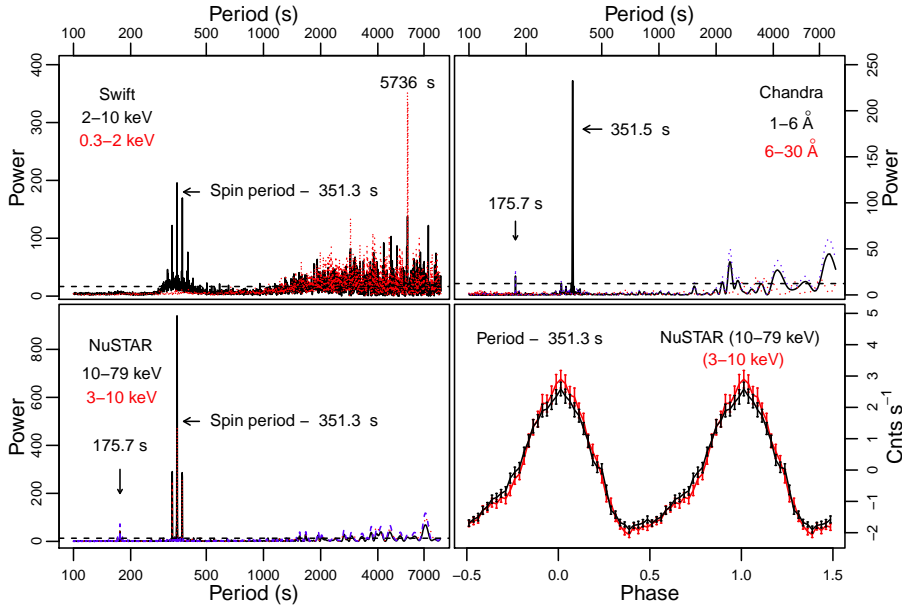


**Figure 3.** Top-left: the LSP of the *Swift* XRT data in the 2–10 keV energy range (black) and at 0.3 – 2 keV (red). Top-right: the LSP of the *Chandra* HETG data in the energy range 1–6 Å before (red) and after (blue) subtracting the highest peak, at 351.5 s. The red line shows the LSP of the *Chandra* HETG data in the energy range 6–30 Å. Bottom-left: the LSP of the *NuSTAR* data in the 10 – 79 keV (black) and 3 – 10 keV (red) energy range. The blue line shows the LSP of the *NuSTAR* data in the 10 – 79 keV range after subtracting the peak at 351.3 s. The horizontal dashed lines show the 0.3% false alarm probability level at all the LSPs. Bottom-right: the *NuSTAR* light curve in the 3 – 10 keV (red) and 10 – 79 keV (black) ranges, folded with the WD spin period of 351.3 s

### 4.3 Evolution of the spin pulse profile with the *Swift* XRT.

The next step was to explore the spin modulation of the light curves. We first investigated how the spin pulse profile changed as the outburst developed. Since the modulation is mostly seen in hard X-rays, we combined the *Swift* XRT light curves above 2 keV in groups of three exposures and

folded them with the 351.3 s period using a constant number of bins. The result is shown in fig. 4: the pulse profile becomes smoother with time and stabilized by day  $\sim 20$  after the beginning of the outburst in optical. The pulse amplitude also depends on the mean value of the count rate. This will be further explored using the *NuSTAR* data.

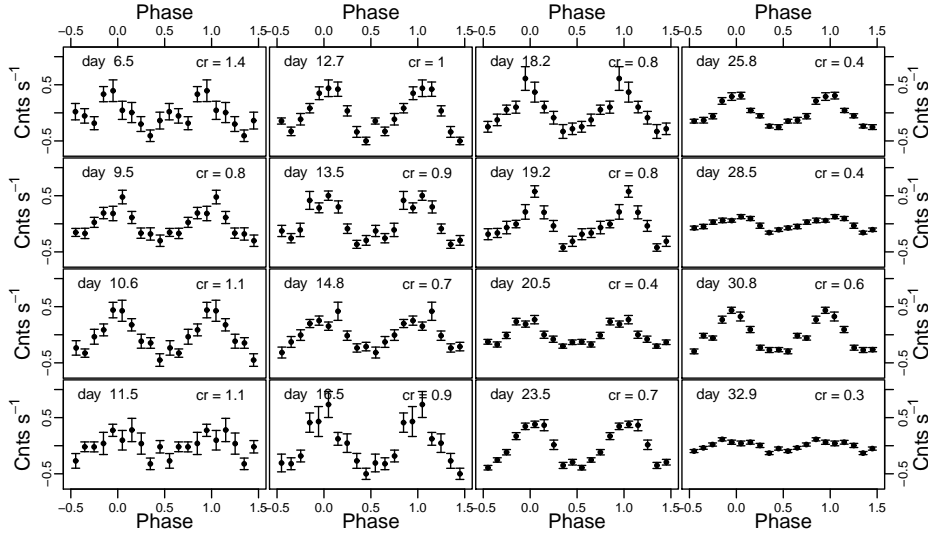


**Figure 4.** Evolution of the spin pulse profiles in the *Swift* XRT light curves above 2 keV. We combined every three individual observations and folded them with the 351.3 s period. The mean date of observation and the mean count rate (cr) is marked on each plot.

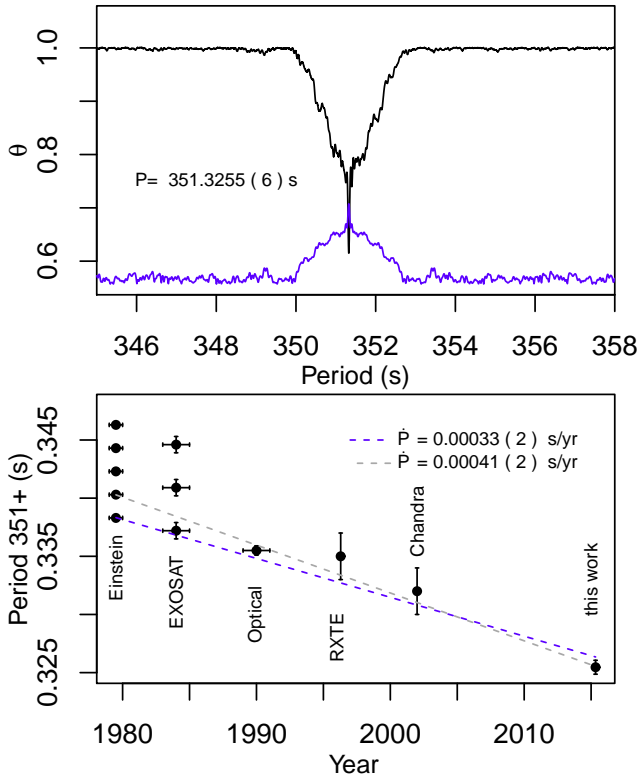


**Figure 5.** Top: PDM analysis of the *NuSTAR*, *Chandra* HETG 1–6 Å and hard *Swift* XRT light curves. Bottom: the WD spin period as a function of time and the result of the linear fitting.

#### 4.4 WD spin-up rate.

We measured the spin period more precisely combining the *NuSTAR*, *Swift* XRT light curve extracted above 2 keV and the *Chandra* HETG light curve in the 1–6 Å wavelength

range. Since the spin amplitude in each instrument is a similar fraction of the mean count rate, and the mean count rate is much lower for *Swift* XRT and the *Chandra* HETG, we first normalized the light curve from each instrument to its mean count rate. In order to account for possible long-term variability we removed linear trends from each segment the *NuSTAR* light curve, from the *Chandra* light curve and from each *Swift* observation before applying the phase dispersion minimization (PDM) method (Stellingwerf 1978). Fig. 5 shows that the PDM analysis resulted in a value of the spin period  $P_{\text{spin}} = 351.3255(6)$  s. Combining the WD spin measurements performed by Eracleous et al. (1991); Watson et al. (1985); Norton et al. (1988); Patterson (1991); Hellier et al. (2004); Mauche (2004) and following a discussion by Patterson (1991) and Mauche (2004), we fitted the trend of  $P_{\text{spin}}$  as a function of time with a linear function. The uncertainty in the spin-up rate is due to the uncertainty in the period derived from the *Einstein* data: two different values, 351.3383 and 351.3403 s, resulted in an acceptable fit, and adopting each of them yields a spin-up rate of 0.00033(2) s yr<sup>-1</sup> and 0.00041(2) s yr<sup>-1</sup>, respectively.

Using the new value of the spin period ( $P_{\text{spin}} = 351.3255(6)$  s), we also calculated the ephemeris of the pulse maxima. The Modified Barycentric Julian Date (MBJD) of the maxima can be found as:

$$T_{\text{max}}(\text{MBJD}) = 57093.51666(21) + 0.004066267(7) * E \quad (1)$$

#### 4.5 Orbital variability of the spin period.

Watson et al. (1985) pointed out that the spin period should be modulated with the orbital one (i.e. X-ray radial velocity curve), but taking into account the estimates of the binary parameters of GK Per, the authors concluded that these variations would be below the detection limit. With the most recent measurements of the mass ratio  $q$ , WD mass  $M_{\text{WD}}$ , binary inclination angle  $i$  and orbital period  $P_{\text{orb}}$ , we derived the expected amplitude of variation of the pulse period  $\Delta P_{\text{spin}}$  with orbital phase. The semi-major axis of the WD's

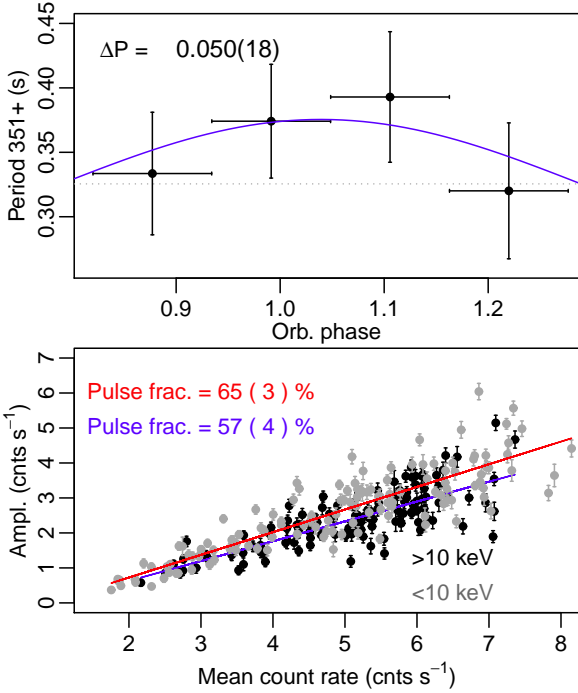


**Figure 6.** Top: the WD spin period as a function of orbital phase and the result of the fit with a sine function. The dashed grey line shows the mean period, 351.3255 s. Bottom: the amplitude of pulses, calculated as (maximum-minimum)/2, as a function of the mean count rate per pulse and the result of the linear fit. The grey dots and red line correspond to the *NuStar* light curve, extracted below 10 keV, and the black dots and blue line — above 10 keV.

orbit is:

$$a_x \sin i = \frac{P_{\text{orb}}}{2\pi} K_x \quad (2)$$

where  $K_x$  is the radial velocity semi-amplitude. Assuming a circular orbit (Crampton et al. 1986) we can write:

$$M_2 \sin^3 i = \frac{P_{\text{orb}} K_x^3}{2\pi G} \left(1 + \frac{1}{q}\right)^2 \quad (3)$$

Using  $q = M_2/M_1$  and equation 3 we obtain the semi-major axis in light-second:

$$a_x = \frac{q}{c} \left[ \frac{P_{\text{orb}}^2}{4\pi^2} \frac{GM_{\text{WD}}}{(1+q)^2} \right]^{1/3} \text{ light-second} \quad (4)$$

where  $c$  is the speed of light. Thus, we finally obtain  $\Delta P_{\text{spin}}$  as:

$$\Delta P_{\text{spin}} = \frac{2\pi P_{\text{spin}}}{P_{\text{orb}}} a_x \sin i \text{ s} \quad (5)$$

Using the measurements of Morales-Rueda et al. (2002) and Suleimanov et al. (2016) ( $q = 0.55 \pm 0.21$ ,  $M_{\text{WD}} \geq 0.86 \pm 0.02 M_{\odot}$ ,  $P_{\text{orb}} = 1.9968 \pm 0.0008$  d) we find that  $a_x \sin i = 6.1 \pm 1.8 \sin i$  lt-sec and  $\Delta P_{\text{spin}} = 0.078 \pm 0.023 \sin i$  s. Since the binary inclination lies within the range 50–73° (Morales-Rueda et al. 2002), the result is  $\Delta P_{\text{spin}} = 0.042 - 0.096$  s. Thus, the orbital modulation of the spin period significantly affects the measurements of the latter

if the observations last for a shorter time than the orbital period. In fact, in fig. 3 we show that the spin period derived from the *Chandra* observation, which is the shortest one, is measured to be longer.

In order to explore a possible spin period variation with the orbital period in our data we combined the *NuSTAR* and the *Chandra* HETG 1–6 Å light curves, both covering half of the orbital period. Since the light curves show also variability on a kilosecond time-scale (see fig. 2) we fitted and subtracted 5-order polynomial functions from light curve segments lasting 14 rotation periods each. The resultant, “flat” light curve, was then divided in four parts of equal length and the spin period was measured in each part with the PDM method.

Unfortunately, we only have the ephemerides of Morales-Rueda et al. (2002), obtained almost 20 years ago, so the error on the phase determination may make it non significant. However, the orbital period itself is precisely measured, and in fig. 6 we show that  $P_{\text{spin}}$  is indeed variable. Fitting its orbital period dependence with a sine function, we find  $\Delta P_{\text{spin}} = 0.050(18)$  s. This is close to the lower limit of the expected range of  $\Delta P_{\text{spin}}$ . We note, however, that flickering cannot be removed, so the uncertainty in this measurement is large.

We applied the template fitting method described in Kato et al. (2009) to the *NuSTAR* light curves extracted above and below 10 keV in order to measure the pulse fraction. We folded the light curves with the 351.3255 s period, fitted the mean pulse profile with a spline function and then used this spline template to fit individual pulses and to measure the amplitude and the mean count rate per pulse. The pulse amplitude was calculated as (fitted pulse maximum - fitted pulse minimum)/2. The bottom panel of fig. 6 shows the result. The correlation between the mean count rate and the amplitude of pulse is very prominent and can be fitted with a linear function, providing values of the pulse fraction of 65 and 57% for the soft and hard light curves, respectively. Variation of the mean count rate reflects the long term variability on the time-scale of kiloseconds (QPOs). The spin modulation is due to the geometric effects and the linear dependence between the mean count rate and the pulse amplitude suggests that QPOs in the *NuSTAR* energy range are due to the intrinsic variability of the emitting source.

## 5 SPECTRAL ANALYSIS

The X-ray spectrum of GK Per is very complex. The long-term observations with *Swift* showed that it is also quite variable, as demonstrated by the hard and soft X-ray light curves in fig. 1. Fig. 7 shows the comparison of the *Swift* XRT spectra obtained on different days, including only spectra with at least 14 data points after we binned the PC mode spectra with a minimum of 20 counts per bin, and the WT mode ones with at least 40 counts per bin. We divided the measurements by the response effective area, so the WT and PC mode spectra could be directly compared. Since all the exposures were longer than the spin period, rotation dependent variability is smeared out. In order to look for possible orbital phase dependence of the spectrum we marked the corresponding orbital phase (from the ephemerides in Morales-Rueda et al. 2002) in each panel. We also labelled

each panel with the mean count rate. We did not find significant spectral variability dependent on the orbital phase, although all the spectra were different from day to day, sometimes with a narrow minimum around 2 keV, other times with a flatter shape around this value. Because of these variations there was no possibility to perform a simultaneous fit of the *Swift* XRT data and the data from the *Chandra* and *NuSTAR* observations and we will discuss these observations separately.

From the timing analysis we found that there are at least two different sources of X-ray emission in GK Per: one dominates above 2 keV and originates somewhere close to the WD, since the flux in this range is modulated with the WD spin period, and the second source, dominating below 2 keV, is visible during the whole spin cycle. We first analysed the hard portion of the X-ray spectrum using the *NuSTAR* and *Chandra* HETG observations. The *Chandra* HETG spectra, having higher energy resolution provide better constrain on the metallicity and the structure of the Fe K complex, while the *NuSTAR* data allow us to measure the shock temperature.

### 5.1 The hard X-ray spectral component.

Hard X-ray emission of accreting magnetic CVs originates in their accretion columns, where the post-shock plasma is cooling mostly via bremsstrahlung radiation and K and L shell line emission as it settles on to the surface of a WD. Therefore, for the hard continuum we used the cooling flow model `mkcflow`, which calculates a plasma in collisional ionization equilibrium (CIE) with a range of temperatures. `vmcflow` model is a modification of the `mkcflow` with variable abundances of individual elements. This model was originally created for clusters of galaxies (Mushotzky & Szymkowiak 1988) but can also be applied to CVs (Mukai et al. 2003). The highest plasma temperature (the shock temperature) is an important parameter for magnetic CVs, allowing to estimate the WD mass (Aizu 1973). The emissivity function in the `mkcflow` model is the inverse of the bolometric luminosity and the model’s normalization constant is the mass accretion rate. In order to investigate the hard X-ray emission, we attempted a simultaneous fit of the *NuSTAR* spectra and the *Chandra* HEG+MEG spectra above 2.5 keV. The *NuSTAR* FPMA and FPMB spectra were fitted together, but the FPMB model was multiplied by a constant to account for a slightly different response of the two detectors. We used the `vmcflow` model to test the abundances. The value of the interstellar absorption was obtained from the reddening  $E(B - V) = 0.3$  (Wu et al. 1989) and the  $nH - E(B - V)$  relation from Bohlin et al. (1978). The shape of continuum above 2 keV indicates that the emission is highly absorbed, but even with partially covering absorber we could not fit the data. A better result was obtained with the `pwab` model (Done & Magdziarz 1998), in which the fraction of X-rays affected by a given column density  $N(H)$  is a power-law function of  $N(H)$  with index  $\beta$ . We fix the lower temperature of the `vmcflow` model to the lowest possible value — 0.0808 keV because a heavily absorbed spectrum like that of GK Per does not allow us to determine it accurately, and physically we expect it to be equal to the white dwarf photospheric temperature.

We also added a Gaussian component to fit the Fe K $\alpha$

fluorescent line at 6.4 keV. The model’s parameters of the best fit are in table 3. The *NuSTAR* and the hard part of the *Chandra* spectrum together with the described model are presented in fig. 8. The inset shows the Fe complex measured in the *Chandra* HEG spectrum. The model slightly underestimates the flux in the forbidden line of the Fe XXV triplet, which may indicate contribution of the photoionization processes. There are also residuals around 6.2–6.3 keV, suggesting Compton-down-scattering of photons. A similar “shoulder” of the Fe K $\alpha$  line was detected in previous *Chandra* HETG observations of GK Per (Hellier & Mukai 2004).

We used the same procedure of the template fitting, described in the previous section, to find the pulse maxima and to extract the on-pulse and off-pulse *NuSTAR* spectra. Assuming that the pulse maximum is at  $\phi=0.5$ , we chose time intervals corresponding to the 0.3 – 0.7 and 0.8 – 1.2 spin phases and used them to extract the on-pulse and off-pulse *NuSTAR* FPMA spectra. These spectra are shown in fig. 9 in comparison with the mean one. All three spectra are remarkably similar. We fitted the on-pulse and off-pulse spectra applying the best-fitting model described above, freezing the maximum plasma temperature, metallicity and the Fe K $\alpha$  line width. The best-fitting parameters in table 3 show that the variation between the on-pulse and off-pulse spectra is due to the normalization of the cooling flow component.

### 5.2 The *Chandra* observation.

We analysed the spectrum below 2 keV focusing on the *Chandra* HETG data to investigate the emission lines ratio and to derive conclusions about the plasma temperature and density and about the mechanism of ionisation. Useful indexes of the plasma properties are the  $R=f/i$  and  $G=(f+i)/r$  ratios, where  $r$ ,  $i$  and  $f$  are the fluxes in the resonance, intercombination and forbidden lines of the He-like triplets, respectively, and the ratios of H-like to He-like resonance lines of the same species (Gabriel & Jordan 1969).

We fitted all the emission lines in the *Chandra* MEG spectrum with Gaussians, assuming that the Ne, Mg and Si lines are absorbed only by the interstellar absorption, and we used a power law to represent the level of continuum. We also assumed that the widths of the lines within a triplet were constant and fixed the distances between these lines to the table values. For the Gaussian fit of the Fe K complex in the *Chandra* MEG we also introduced the `pwab` model with the parameters of the fit of the mean *NuSTAR* spectrum and a bremsstrahlung component at  $kT=14$  keV for the underlying continuum. We did not find any significant line shifts departing from the laboratory wavelengths. The resulting broadening and flux are presented in table 4 and in fig. 10. We also measured the  $R$  and  $G$  ratios for the Si, Mg and Ne triplets, and give them in table 5.

The  $G$  ratio is around 2, which means that there is no strong photoionizing component (in the case of pure photoionized plasma  $G$  is  $\sim 4$ ). We either have a collisional-ionization mechanism or a ‘hybrid plasma’, a mixture of collisional and photoionization (Porquet & Dubau 2000). The He-like triplets of different elements show very different line ratios. The Si XIII triplet has a very strong forbidden line, which cannot be explained solely with collisional ionization, while Mg XI and Ne IX have quite weak forbidden lines, but

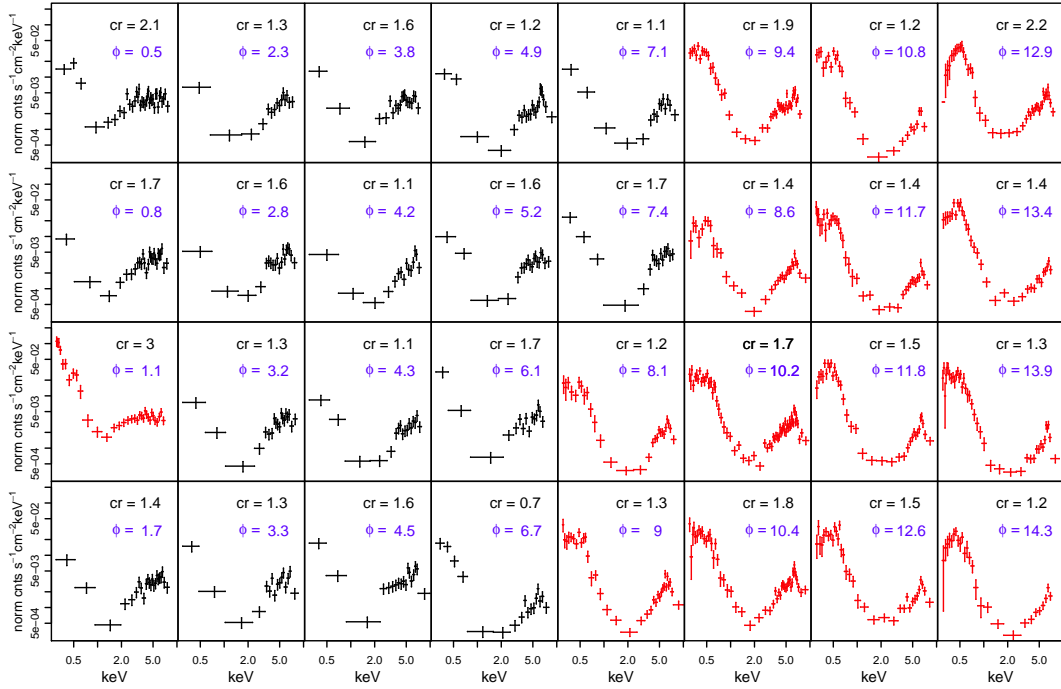


**Figure 7.** Evolution of the Swift XRT spectra of GK Per with time. The black points are data obtained in the PC mode and the red ones in the WT mode. The mean count rate and the corresponding orbital phase are marked on each panel.

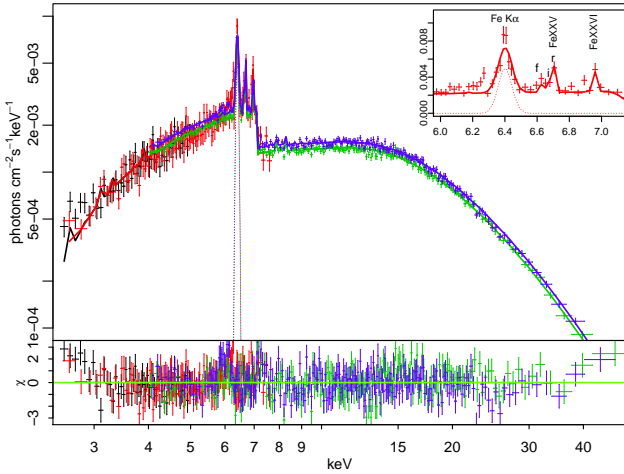


**Figure 8.** The unfolded *NuSTAR* FPMA (blue), FPMB (green), *Chandra* MEG (black) and HEG (red) spectra and the best-fitting model. The model components are marked with the dashed lines. The inset shows the Fe complex in the *Chandra* HEG spectrum.

very strong intercombination lines, which indicates a high density (Porquet & Dubau 2000).

Mukai et al. (2003) showed that the *Chandra* HETG spectrum of GK Per obtained during the outburst in 2002 is consistent with the predictions of a photoionization model with a power law as the photoionizing continuum. Although the power law emission gave a good approximation, and could indeed photoionize the plasma in which the soft X-rays emission lines are produced, such a non thermal component in a CV does not seem to have a physical reason. Given also the G ratio and the absence of a clearly non-

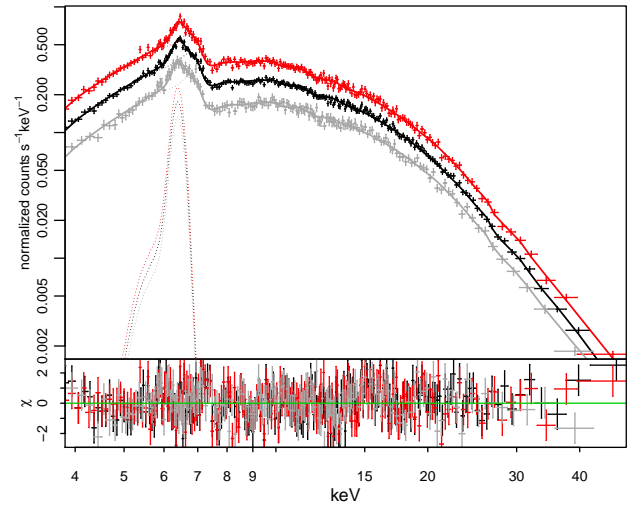


**Figure 9.** The *NuSTAR* FPMA mean (black), on-pulse (red) and off-pulse (grey) spectra and the best fitting model. The model components are marked with the dashed lines.

thermal component in the *NuSTAR* range, we do not favour this explanation for the present set of observations.

The top panel of figure 11 shows the comparison of the *Chandra* MEG spectrum obtained in 2015 with *Chandra* MEG data discussed in Mukai et al. (2003). The most recent spectrum of GK Per has much weaker lines in the region above 20 Å, which is due to contaminant build-up of the *Chandra* HETG+ACIS detector. The low energy effective area is reduced in 2015 compared to 2002. The intensities of the lines that are in the 6–11 Å region are almost the same. The *Chandra* spectra in fig. 11 give an additional proof that

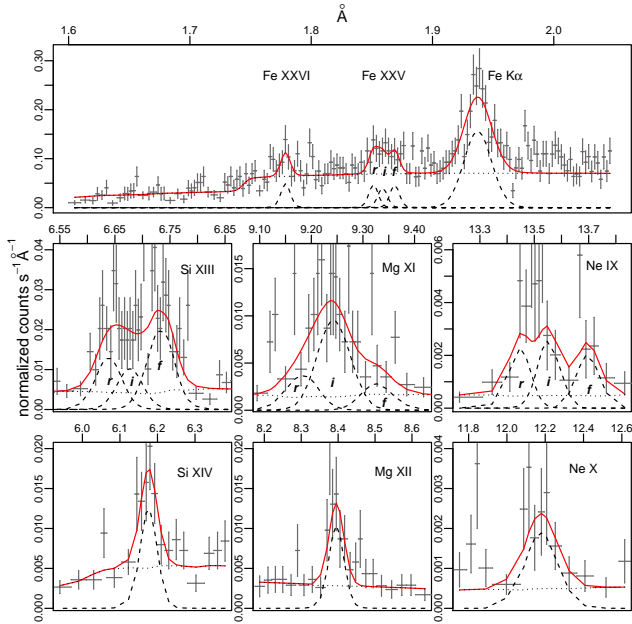


**Figure 10.** Gaussian fits of the strongest emission lines of the *Chandra* HEG (top) and MEG spectra. In the fits we assumed that the value of  $\sigma$  is the same within a triplet. The distances between the lines in a triplet were fixed to the table values. The values of  $\sigma$  of the Fe XXVI and Fe XXV<sub>r,f,i</sub> lines were fixed to the instrument resolution.

there are several distinct sources of emission: there is no correlation between the 6–11 Å emission lines strengths and the hard continua below 5 Å.

The N VII line detected in the *Chandra* MEG 2002 and 2015 spectra showed remarkably different profiles in comparison to the other lines. The N VII line’s regions are shown in fig. 12. In March 2002 and April 2015 two different emission lines were resolved around the rest-frame position of N VII, while in April 2002 another blue-shifted component could be distinguished. Table 6 shows the central positions and the unabsorbed fluxes of all the lines that were resolved in three *Chandra* MEG spectra. Vrielmann et al. (2005) in their Reflection Grating Spectrograph (RGS) spectrum of GK Per also noticed that the N VII line had a different structure that could be approximated by three Lorentzian profiles. Two scenarios could explain these emission lines. It can be one central N VII line and one/two N VII lines shifted from the main line. Another possibility is that the line around 24.8 Å is indeed the N VII emission, but the line around 24.9 Å is the N VI He $\beta$  line, both with zero velocity. From the *Chandra* MEG spectra we find that if the lines around 24.8 Å are different components of the central N VII line, this would indicate velocity shifts of 1200 – 1600 km s<sup>-1</sup>. Similar red and blue-shifted emission line’s components, although with smaller velocity shifts, were measured in the optical spectra of GK Per during outbursts (Bianchini et al. 2003) and were attributed to the emission from the matter in the magnetosphere, falling on to the WD. A question to answer is why N VII is the only line that shows such a complex profile. Two *Chandra* MEG spectra obtained near optical maximum of the same outburst (see tab. 6) also clearly show that the flux of the different N VII line’s components varies with time,

while the flux of central line is stable within the errors. If we observe, instead, the N VII and N VI He $\beta$  emission lines the relative intensities of the two lines can be used as temperature indicator (under the assumption of collisional ionization equilibrium). The different relative intensities in March and April of 2002 would imply that the temperature changes. The very strong N VI He $\beta$  line in comparison to N VII in the 2015 spectrum indicates also a very low plasma temperature:  $\lesssim 0.08$  keV.

We checked whether the expanding nova shell can contribute to line emission in soft X-rays. Balman (2005) showed that the shell has enhancement in the elemental abundances of Ne and N and Vrielmann et al. (2005) fitted the quiescence *Chandra* ACIS-S spectrum of the shell with pure emission lines of N, O and Ne, although the lines could not be resolved. In order to estimate a possible contamination of the N VII line from the central source by the shell emission, we compared the predictions of the shell emission model from Takei et al. (2015) with the 2015 *Chandra* MEG spectrum. The model from Takei et al. (2015) with the only modification in the N abundance (we assumed N/N<sub>⊙</sub>=5) and a power law to represent the continuum level is shown with the red line in the bottom panel of fig. 12. We see that the N VII/N VI line’s flux from the entire shell is much smaller than that measured in the 2015 *Chandra* MEG spectrum. We conclude that the N lines around 24.8 Å originate not from the extended shell, but the nature of the different components is unknown.

The complexity of the spectrum is demonstrated by the ratios of H to He-like lines, which in the case of pure collisional ionization is a signature of the plasma temperature. The He-like lines are stronger than the H-like for all the species. The Si XIII to Si XIV lines ratio indicates a temperature  $\sim 0.9$  keV, so the origin of these lines is not in the hotter plasma that explains the *NuSTAR* spectrum. The He to H-like lines ratios of Mg and Ne correspond to even lower plasma temperatures. These lines also cannot be explained by another *mkcflow* component at lower temperature since the cooling flow model always produces H-like lines stronger than the He-like lines (Luna et al. 2015). The middle and bottom panels of fig. 11 show the comparison of the *Chandra* MEG spectrum with the predictions of the single temperature thermal plasma emission model. We added to the best-fitting model of the *NuSTAR* data a *vappec* component (a single-temperature plasma in CIE with variable abundances of individual elements) and a Gaussian at 0.5 keV to represent the N VII line. Following Vrielmann et al. (2005) and Evans et al. (2009b) we also introduced a blackbody component to represent the thermalized X-ray emission from the WD surface at kT = 66 eV. The choice of the blackbody temperature will be explained in the next section. In the middle panel of fig. 11 the temperature of the *vappec* component was fixed to 0.9 keV, in order to fit the Si XIII to Si XIV lines ratio. In this case the model underestimates the level of continuum and overestimates the He to H-like lines ratios of Mg and Ne. In the bottom panel the temperature of the *vappec* component corresponds to the best-fitting value — 4.9 keV, which correctly estimates the level of continuum, but cannot reproduce the line ratios. A lower temperature *vappec* component with higher normalization constant affected by a complex absorber could explain the Si lines and the continuum level, but not the He to H-like lines ratio of Mg and Ne. The emis-

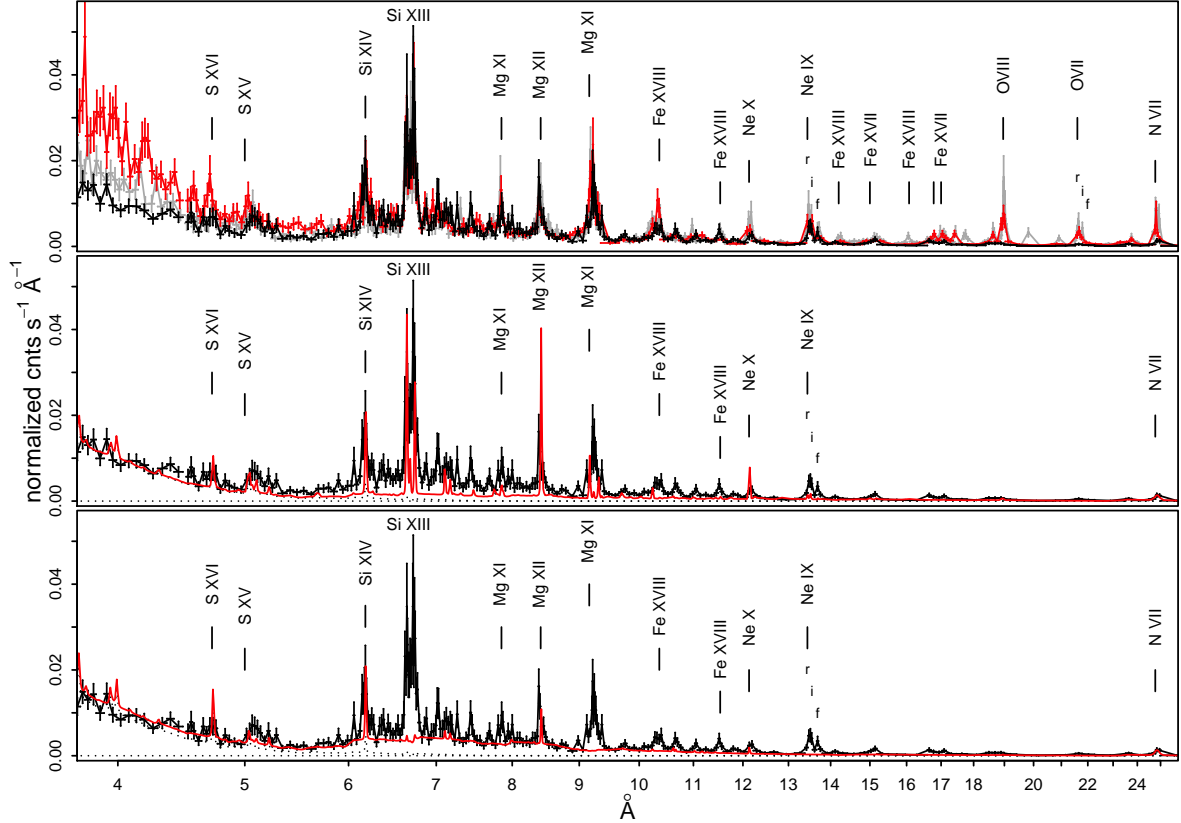


**Figure 11.** From top to bottom: comparison of the *Chandra* MEG spectra of GK Per in outbursts in 2015 and 2002. The *Chandra* MEG spectrum discussed in this paper is plotted in black, while the *Chandra* MEG spectra obtained on March 27 and April 9 2002 (PI: C. Mauche) are plotted in red and grey, respectively. All the observations were performed close to the optical maxima. Middle panel: the 2015 *Chandra* MEG spectrum and the  $\text{TBabs} \times (\text{pwab} \times (\text{vmcflow} + \text{gaussian}) + \text{vapec} + \text{bb} + \text{gaussian})$  model (the red line). The temperature of the *vapec* component was fixed to 0.9 keV. Bottom panel: The 2015 *Chandra* MEG spectrum with the same model and the 4.9 keV temperature of the *vapec*.

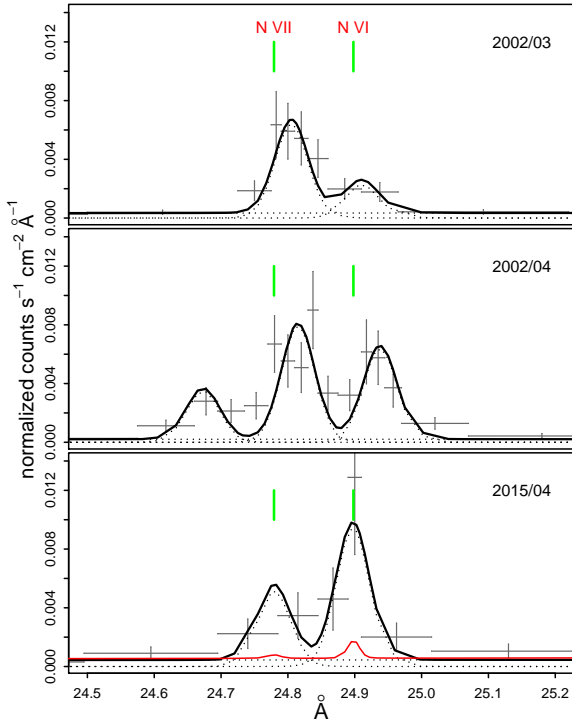
sion lines ratios clearly indicate a multi-temperature plasma emission. However, we added another *apc* component to fit the lines at longer wavelengths, but it did not improve the fit significantly. Fig. 11 also shows that the *vapec* model underestimates the intercombination and forbidden lines in all the triplets. Thus, the overall spectrum below 2 keV cannot be represented with a model of plasma in CIE, not with a cooling flow, neither with single or two-temperature *vapec* model.

Fig. 8 in Porquet & Dubau (2000) shows that the temperature of 0.9 keV and the value of the R ratio of the Si triplet (see table 5), which is a density indicator, corresponds to the electron density  $n_e \sim 3 \times 10^{13} \text{ cm}^{-3}$ . Using these estimates and the value of normalization of the *vapec* component (which gives the emission measure) we find that the radius of the emitting source is  $\sim 1.4R_{\text{WD}}$ , assuming a spherical distribution of the emitting plasma,  $M_{\text{WD}}=0.86 M_{\odot}$  and a WD mass-radius relation from Nauenberg (1972). It should be mentioned, however, that the G and R ratios are measured with large uncertainty (see table 5) and we cannot evaluate the contribution of photoionization processes, so this is a qualitative estimate.

### 5.3 *Swift* XRT observations

Fig. 13 shows the comparison of the average *Swift* XRT spectra in the first two weeks and in the following two weeks. The soft flux increased with time, while the hard flux decreased. We fitted the average spectra with the model described in section 5.2 in order to estimate the changes of the flux in different spectral regions. There was no possibility to measure the Fe  $K\alpha$  line width in the *Swift* spectra, so we fixed its central position and the  $\sigma$  to the values from tab. 3. We assumed that the metallicity did not change with time and the corresponding parameters in the *vapec* component were constrained to be the same in the two data sets. The best-fitting parameters are listed in the table 8. Here and in the following sections we refer to the spectral regions as soft (blackbody-like, below 0.8 keV), intermediate (between 0.8 and 2 keV) and hard (cooling flow component, above 2 keV). There are significant residuals in the part of the spectra below 2 keV and in particular below 0.4 keV in the spectrum obtained in the later period. There is also an excess around 0.9 keV, where the Ne IX line is.

Although the model is quite approximate, we concluded that the hard X-ray flux decreased mostly because of the increased absorption. The soft X-ray flux increased, first of all because of the increased normalization of the blackbody



**Figure 12.** Comparison of the N VII emission line’s profile measured with the *Chandra* MEG in 2015 and 2002 (the data sets are the same as in fig. 11). The dates of observations and the rest-frame positions of the N VII and N VI He $\beta$  lines are marked at each panel. All the lines were fitted with two or three Gaussians and a power law to represent the continuum level. In the bottom panel we also show the contribution from the nova shell, based on the model of [Takei et al. \(2015\)](#) and a power law to fit the underlying continuum.

component and the `vapcc` components. The blackbody emitting area increased by a factor of 3, but it remained of the order of  $10^{-5} - 10^{-6}$  the area of the WD surface, which is the typical size of a heated polar region in soft IPs (see e.g. [Bernardini et al. 2012](#)).

## 6 DISCUSSION

### 6.1 The WD spin and the long-term variations.

The *NuSTAR* observations of GK Per provided the first detection of a high amplitude modulation due to the WD spin period in X-rays above 10 keV in an IP (only XY Ari in outbursts is known to show a comparable amplitude of modulation). The fact that the spin modulation is so strong in hard X-rays and that the pulse amplitude is not energy dependent indicates that the modulation is a geometric effect rather than due to absorption as in the majority of IPs. This modulation can be partially explained by an obscuration of the lower accretion pole by the inner disc ([Hellier et al. 1997, 2004](#)). However, the obscuration of the lower pole alone, does not explain the pulse profile. A small shock region with a low shock height will either be completely visible or completely behind the white dwarf with very little transition in between, resulting in a square wave spin modulation. In the case of GK Per the modulation is not a square wave but quasi-

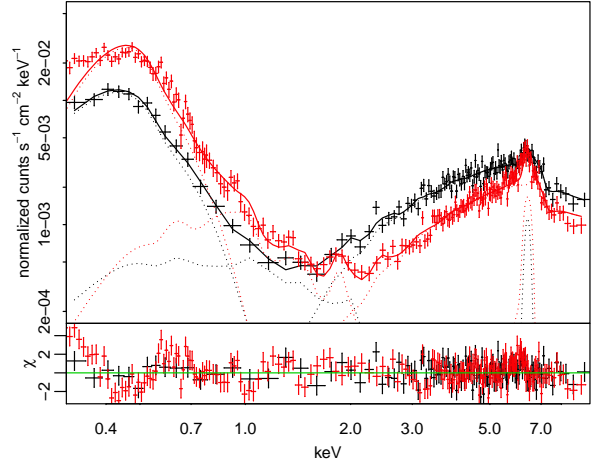


**Figure 13.** The averaged *Swift* XRT spectra obtained during the first (black) and the second two weeks (red) of the observations and the best-fitting model. The model parameters are plotted with the dotted lines.

sinusoidal and about 40% of the total flux is always visible, suggesting a large shock height or an extended shock region. In the first case the soft X-rays, originating closer to the WD surface, will show more prominent modulation, while the hardest X-rays — just moderate eclipses. In GK Per the pulse profiles are not energy dependent, and the pulse fraction is almost the same above and below 10 keV, so we can reject this possibility. In GK Per we most probably deal with an accretion curtain whose footprint is much extended and forms an arc that covers 180 deg. The fraction of the arc that is visible can vary smoothly, resulting in only moderate energy dependence of pulses. It is consistent with the idea proposed by [Hellier et al. \(2004\)](#) and [Vrielmann et al. \(2005\)](#) that in outburst accretion flows to the poles from all azimuths.

Variability on the time-scale of 7000 s was also detected even above 10 keV and this cannot be explained by the model of [Hellier et al. \(2004\)](#), in which the QPOs are due to absorption by bulges of material in the accretion disk. These variations are most probably intrinsic variability of the accretion column emission due to inhomogeneous accretion. This is supported by the linear dependence between the mean X-ray count rate and the pulse amplitude.

We have also shown that, although the hard X-ray emission shows a very prominent and high-amplitude spin modulation, precise measurements of the spin period are not so straightforward due to the presence of flickering and the orbital-related variability. The *NuSTAR* and *Chandra* data alone did not allow us to measure the spin period precisely, and only the long monitoring with *Swift* helped to estimate the spin-up rate.

### 6.2 Hard X-ray component.

The spectrum above 2 keV can be well fitted with the cooling flow model with maximum temperature of 16.2 keV, representing the emission from the WD accretion column. The continuum indicates that the source is highly absorbed, and this is also supported by the fact that the contribution of the cooling flow component to the observed line emission below

2 keV should be negligible. The source of this absorption most probably is the pre-shock material. Since, depending on the spin phase there will be different amount of absorption in our line of sight, the overall picture is very complex, and is best approximated by the `pwab` model.

The shock temperature derived from the fit is lower than that observed in quiescence and at the beginning of the outburst, which is about 26–27 keV (Ishida et al. 1992; Brunschweiler et al. 2009; Yuasa et al. 2016). When the inner radius of the accretion disc shrinks, the shock temperature is reduced by a factor of:

$$f = T_o/T_q = (1 - r_{M_o}^{-1})/(1 - r_{M_q}^{-1}) \quad (6)$$

(Suleimanov et al. 2005), because the approximation of the free fall velocity cannot be used anymore (here  $r_{M_o}$  and  $r_{M_q}$  are the outburst and quiescent radii of the magnetosphere in the units of the WD radius). The magnetospheric radius is defined by a balance between the ram pressure in the disk, which depends on mass transfer, and the magnetic pressure. As long as the optical flux is increasing, we expect the mass transfer to be constantly increasing as well, since the optical probes the portion of the disc involved in the outburst. This should result in gradual shrinking of the inner disc radius and lowering of the shock temperature. The observations in the very first days of the outburst (Yuasa et al. 2016) demonstrate that the decrease of the temperature indeed does not happen immediately. However, the spectral resolution of the short *Swift* exposures and the uncertainty in the intrinsic absorption did not allow us to trace this process. Even in the fit to the averaged *Swift* XRT spectra the errors of the plasma temperature are too high to measure the difference.

### 6.3 Intermediate energy X-ray spectrum

These are the key points of the analysis of the intermediate X-ray spectral component (0.8–2.0 keV):

- There are very prominent emission lines of Si, Mg, Ne and Fe XVII–Fe XVIII.
- The emission lines did not show any systematic velocity shift or broadening.
- The emission line ratios do not allow to clearly distinguish between collisional and photoionization mechanisms.
- Assuming collisional ionization equilibrium, the continuum below 2 keV is produced in a medium with a higher temperature than the emission line ratios indicate.
- The spectrum in the 0.8–2 keV range cannot be represented with a model of plasma in CIE, not with a cooling flow, neither with single or two-temperature `vapec` model.
- Neither the continuum nor the emission lines show any spin modulation in this energy range.

Vrielmann et al. (2005) claimed that the emission lines in the X-ray spectrum of GK Per originate in the magnetosphere of the WD, because they show no rotation-related modulations. We found that not only the lines, but also the underlying continuum is not modulated, indicating that the source of emission is not confined to the WD polar regions. This conclusion is also supported by the estimates of the size of the emitting region, which is of the same order of magnitude as the estimated magnetospheric radius of GK Per by Suleimanov et al. (2016) (1.4  $R_{WD}$  and 2.8  $R_{WD}$ ).

We propose that the magnetospheric boundary is the emission site of the intermediate spectral component and the intermediate energy X-ray flux is related to the decrease of the shock temperature. If the shock temperature during outbursts is 2/3 of that in quiescence (Brunschweiler et al. 2009; Suleimanov et al. 2016), half of the remaining energy is radiated away in the Keplerian disk. Where is the remaining 1/6th irradiated and how do we explain the energy budget? The site of emission may thus be the magnetospheric boundary, producing this intermediate X-ray spectral component, in the 0.8–2 keV range, even if the exact mechanism of emission is not clear yet. This idea partially explains the anticorrelation of the soft and hard X-rays during the outburst: the lower the shock temperature, the more energy is released in the magnetospheric boundary as moderately soft X-ray emission. Additionally, Suleimanov et al. (2016) measured the magnetospheric radius using the observed break frequency in the power spectrum and found  $\nu_{\text{break}} = 0.0225 \pm 0.004$ , corresponding to the Keplerian velocity of  $\sim 2500 \text{ km s}^{-1}$ , much faster than at the co-rotation radius, suggesting that the material in the disc must lose energy in order to decelerate and follow the field lines.

### 6.4 The soft component.

The spectral fits and the comparison of the *Chandra* data obtained at different epochs (see fig. 11) indicate at least two distinct sources of emission below 2 keV. However, since there is no proper model for the intermediate energy X-ray spectrum of GK Per, it is quite difficult to disentangle the spectral components. The softest part of the spectrum can indeed be blackbody-like and originate on the surface of the WD, heated by the accretion column. Such blackbody-like component in an X-ray spectrum is a distinct property of “soft intermediate polars” (see e.g. Evans & Hellier 2007; Anzolin et al. 2008). The size of the blackbody emitting region was 0.0026 and 0.0083  $R_{WD}$  (using the mass-radius relation from Nauenberg 1972 and  $M=0.86 M_{\odot}$ ), in the first and the second halves of the monitoring and the temperature was 60 – 70 eV, which is within the range of typical values for soft IPs. The increase of the luminosity of the blackbody-like component indicates that more material is penetrating deeper in the WD photosphere, producing thermalized X-rays emission, which may be an effect of the increased mass accretion rate. The latter reaches maximum around the maximum of the optical light. This is supported by the findings of Šimon (2015), who analysed a sequence of outbursts in GK Per and noticed a discrepancy between the mass transfer through the disc and X-ray emission from the accretion column, which is largest around the optical maximum; this can be explained by a buried shock.

On the other hand, there are significant residuals from the blackbody fit of the *Swift* XRT spectra (fig. 13). Following the discussion from Evans et al. (2009b) we attempted to estimate the upper limit to the temperature of the accretion disc in order to check whether it can contribute to the soft X-ray range. The upper limit to the temperature can be found as:

$$T(R) = \left( \frac{3GM\dot{M}}{8\pi R^3\sigma} \right)^{1/4} \quad (7)$$

(Frank et al. 2002). Using the WD mass-radius relation from

Nauenberg (1972), the values of  $\dot{m}$  from table 3,  $M=0.86 M_{\odot}$  and inner disc radius  $R=2.8R_{\text{WD}}$  (Suleimanov et al. 2016) we find that the disc temperature can be as high as 90 000 K. This peak temperature corresponds to a blackbody peak wavelength of 320 Å. The inner disc region significantly contributes to the FUV and UV ranges, however, this temperature is still low to be detected with the *Swift* XRT (should be at least 150 000 K) and the disc emission cannot explain the very soft-X-ray excess, seen in fig. 13.

Strong emission lines were measured in the *Chandra* HETG spectra obtained in 2002 in a range as soft as 0.5 keV, where the blackbody component dominates, indicating a significant contribution from the low-temperature thin plasma emission. The N VII line at 0.5 keV additionally shows a completely different profile with two to three components, separated by  $\sim 1200\text{--}1600 \text{ km s}^{-1}$ .

## 7 CONCLUSIONS

We have presented the long-term monitoring of GK Per in a broad energy range, from UV to hard X-rays, during the dwarf nova outburst in March-April 2015. The *NuSTAR* observations allowed to detect a large-amplitude WD spin modulation in the very hard X-rays, which is unusual for an IP.

The spectral and timing analysis of our data has revealed three distinct spectral components, evolving during the outburst. The spectrum above 2 keV can be well explained by a cooling post-shock plasma in the accretion column, highly absorbed by a pre-shock material. The spectrum below  $\sim 0.8$  keV probably represents the thermalized X-ray emission from the heated WD surface. The emission line spectrum between 0.8 and 2 keV is the most mysterious, since it cannot be represented by any existing model of plasma in collisional ionization equilibrium. We propose that it originates in the magnetospheric boundary around the WD.

Therefore, as the outburst develops and the mass transfer through the disc grows, there are three simultaneous processes affecting the X-ray spectrum:

- The ram pressure increases at the magnetospheric boundary, pushing the accretion disc towards the WD surface and causing the decrease of the shock temperature.
- The lower the shock temperature with respect to the quiescence level, the more energy is released in the magnetospheric boundary in the  $\sim 0.8 - 2.0$  keV range.
- Increased specific mass accretion rate in the accretion column results in a higher amount of material that penetrates deeper in the WD photosphere, causing the increase of the blackbody-like radiation.

The complexity of the X-ray spectrum, the behaviour in different energy ranges and the discrepancy between the spectra we obtained and some predictions of the existing models make GK Per a challenging target for future studies. We propose that the observational strategy should be to monitor GK Per at different stages of its outburst evolution, in order to disentangle the spectral components and to reveal the contribution from different sources.

## ACKNOWLEDGEMENTS

We acknowledge with thanks the variable star observations from the AAVSO International Data base. This work made use of data supplied by the UK Swift Science Data Centre at the University of Leicester. Polina Zemko acknowledges a pre-doctoral grant of the CARIPARO foundation at the University of Padova. G. J. M. Luna is a member of the “Carerra del Investigador Científico (CIC)” of CONICET and acknowledges support from Argentina grant ANPCYT-PICT 0478/14. Marina Orio acknowledges an award of the *Chandra* X-ray Center-Smithsonian Observatory. Polina Zemko and Marina Orio also acknowledge support of an INAF-ASI *NuSTAR* travel grant awarded in 2015.

## REFERENCES

- Aizu K., 1973, *Progress of Theoretical Physics*, **50**, 344  
 Anupama G. C., Kantharia N. G., 2005, *A&A*, **435**, 167  
 Anzolin G., de Martino D., Bonnet-Bidaud J.-M., Mouchet M., Gänsicke B. T., Matt G., Mukai K., 2008, *A&A*, **489**, 1243  
 Balman Ş., 2005, *ApJ*, **627**, 933  
 Bernardini F., de Martino D., Falanga M., Mukai K., Matt G., Bonnet-Bidaud J.-M., Masetti N., Mouchet M., 2012, *A&A*, **542**, A22  
 Bianchini A., Sabadin F., 1983, *A&A*, **125**, 112  
 Bianchini A., Sabbadin F., Favero G. C., Dalmeri I., 1986, *A&A*, **160**, 367  
 Bianchini A., Canterna R., Desidera S., Garcia C., 2003, *PASP*, **115**, 474  
 Bohlin R. C., Savage B. D., Drake J. F., 1978, *ApJ*, **224**, 132  
 Brunschweiler J., Greiner J., Ajello M., Osborne J., 2009, *A&A*, **496**, 121  
 Burrows D. N., et al., 2005, *Space Sci. Rev.*, **120**, 165  
 Canizares C. R., et al., 2005, *PASP*, **117**, 1144  
 Crampton D., Fisher W. A., Cowley A. P., 1986, *ApJ*, **300**, 788  
 Done C., Magdziarz P., 1998, *MNRAS*, **298**, 737  
 Eastman J., Siverd R., Gaudi B. S., 2010, *PASP*, **122**, 935  
 Eracleous M., Patterson J., Halpern J., 1991, *ApJ*, **370**, 330  
 Evans P. A., Hellier C., 2007, *ApJ*, **663**, 1277  
 Evans A., Bode M. F., Duerbeck H. W., Seitter W. C., 1992, *MNRAS*, **258**, 7P  
 Evans P. A., et al., 2007, *A&A*, **469**, 379  
 Evans P. A., et al., 2009a, *MNRAS*, **397**, 1177  
 Evans P. A., Beardmore A. P., Osborne J. P., Wynn G. A., 2009b, *MNRAS*, **399**, 1167  
 Eyres S. P. S., Salama A., Evans A., Bode M., Dougherty S., Waters B. F. M., Rawlings J. C., 1999, in Cox P., Kessler M., eds, *ESA Special Publication Vol. 427, The Universe as Seen by ISO*. p. 309  
 Frank J., King A., Raine D. J., 2002, *Accretion Power in Astrophysics: Third Edition*  
 Gabriel A. H., Jordan C., 1969, *MNRAS*, **145**, 241  
 Ghosh P., Lamb F. K., 1979, *ApJ*, **232**, 259  
 Hellier C., Mukai K., 2004, *MNRAS*, **352**, 1037  
 Hellier C., Mukai K., Beardmore A. P., 1997, *MNRAS*, **292**, 397  
 Hellier C., Harmer S., Beardmore A. P., 2004, *MNRAS*, **349**, 710  
 Hill J. E., et al., 2005, in Siegmund O. H. W., ed., *Proc. SPIE Vol. 5898, UV, X-Ray, and Gamma-Ray Space Instrumentation for Astronomy XIV*. pp 313–328, doi:10.1117/12.618026  
 Ishida M., Sakao T., Makishima K., Ohashi T., Watson M. G., Norton A. J., Kawada M., Koyama K., 1992, *MNRAS*, **254**, 647  
 Kato T., et al., 2009, *PASJ*, **61**, S395  
 Kim S.-W., Wheeler J. C., Mineshige S., 1992, *ApJ*, **384**, 269

King A. R., Ricketts M. J., Warwick R. S., 1979, *MNRAS*, **187**, 77P

Krimm H. A., et al., 2013, *ApJS*, **209**, 14

Liimets T., Corradi R. L. M., Santander-García M., Villaver E., Rodríguez-Gil P., Verro K., Kolka I., 2012, *ApJ*, **761**, 34

Luna G. J. M., Raymond J. C., Brickhouse N. S., Mauche C. W., Suleimanov V., 2015, *A&A*, **578**, A15

Mauche C. W., 2004, in Vrielmann S., Cropper M., eds, *Astronomical Society of the Pacific Conference Series Vol. 315*, IAU Colloq. 190: Magnetic Cataclysmic Variables. p. 120

McLaughlin D. B., 1960, in Greenstein J. L., ed., *Stellar Atmospheres*. p. 585

Morales-Rueda L., Still M. D., Roche P., 1999, *MNRAS*, **306**, 753

Morales-Rueda L., Still M. D., Roche P., Wood J. H., Lockley J. J., 2002, *MNRAS*, **329**, 597

Mukai K., Kinkhabwala A., Peterson J. R., Kahn S. M., Paerels F., 2003, *ApJ*, **586**, L77

Mukai K., Rana V., Bernardini F., de Martino D., 2015, *ApJ*, **807**, L30

Mushotzky R. F., Szymkowiak A. E., 1988, in Fabian A. C., ed., *NATO Advanced Science Institutes (ASI) Series C Vol. 229*, NATO Advanced Science Institutes (ASI) Series C. pp 53–62

Nauenberg M., 1972, *ApJ*, **175**, 417

Nogami D., Kato T., Baba H., 2002, *PASJ*, **54**, 987

Norton A. J., Watson M. G., 1989, *MNRAS*, **237**, 853

Norton A. J., Watson M. G., King A. R., 1988, *MNRAS*, **231**, 783

Patterson J., 1991, *PASP*, **103**, 1149

Porquet D., Dubau J., 2000, *A&AS*, **143**, 495

Sabbadin F., Bianchini A., 1983, *A&AS*, **54**, 393

Scargle J. D., 1982, *ApJ*, **263**, 835

Shara M. M., Zurek D., De Marco O., Mizusawa T., Williams R., Livio M., 2012, *AJ*, **143**, 143

Stellingwerf R. F., 1978, *ApJ*, **224**, 953

Suleimanov V., Revnivtsev M., Ritter H., 2005, *A&A*, **435**, 191

Suleimanov V., Doroshenko V., Ducci L., Zhukov G. V., Werner K., 2016, *A&A*, **591**, A35

Takei D., Drake J. J., Yamaguchi H., Slane P., Uchiyama Y., Katsuda S., 2015, *ApJ*, **801**, 92

Vrielmann S., Ness J.-U., Schmitt J. H. M. M., 2005, *A&A*, **439**, 287

Warner B., 1976, in Eggleton P., Mitton S., Whelan J., eds, *IAU Symposium Vol. 73, Structure and Evolution of Close Binary Systems*. p. 85

Warner B., 2004, *PASP*, **116**, 115

Warner B., Woudt P. A., 2002, *MNRAS*, **335**, 84

Watson M. G., King A. R., Osborne J., 1985, *MNRAS*, **212**, 917

Williams A. S., 1901, *Astronomische Nachrichten*, **155**, 29

Wu C.-C., Holm A. V., Panek R. J., Raymond J. C., Hartmann L. W., Swank J. H., 1989, *ApJ*, **339**, 443

Yuasa T., Hayashi T., Ishida M., 2016, *MNRAS*, **459**, 779

Simon V., 2015, *A&A*, **575**, A65

This paper has been typeset from a  $\text{\TeX}/\text{\LaTeX}$  file prepared by the author.

**Table 1.** Observational log.

Instrument	Date*	Exp.(s)	Count rate
Swift XRT(PC)	57093.15	606.7	1.72±0.10
	57093.58	1268.7	2.10±0.08
	57094.08	1033.0	1.70±0.08
	57094.68	373.6	1.15±0.10
	57095.04	952.8	2.12±0.13
	57095.93	960.3	1.41±0.07
	57096.30	744.7	1.49±0.09
	57096.90	441.3	1.79±0.14
	57097.04	970.3	1.33±0.08
	57097.57	937.7	0.94±0.06
	57098.03	997.9	1.62±0.09
	57098.97	882.6	1.35±0.07
	57099.17	875.0	1.28±0.07
	57099.57	514.0	1.78±0.12
	57100.11	922.7	1.58±0.08
	57100.97	1033.0	1.08±0.06
	57101.10	1133.3	1.11±0.06
	57101.57	925.2	1.64±0.09
	57102.23	1058.0	1.18±0.06
	57102.86	910.1	1.61±0.09
57103.10	917.7	0.85±0.06	
57103.63	418.7	0.86±0.07	
57104.22	140.4	1.07±0.12	
57104.70	975.3	1.70±0.10	
57105.95	905.1	0.67±0.04	
57106.15	1075.6	1.72±0.09	
57106.76	965.3	1.15±0.07	
57107.29	1110.7	1.71±0.09	
57107.82	1196.0	0.70±0.04	
Swift XRT(WT)	57094.65	497.7	3.01±0.08
	57106.15	28.7	3.6±0.5
	57108.75	985.2	1.24±0.04
	57109.62	986.3	1.43±0.04
	57110.51	1145.6	1.31±0.04
	57111.28	1086.9	1.93±0.04
	57112.85	1877.8	1.69±0.03
	57113.34	1228.2	1.84±0.04
	57114.13	1040.9	1.18±0.04
	57115.90	2401.5	1.35±0.03
	57116.11	10801.0	1.46±0.04
	57117.66	974.1	1.52±0.04
57118.20	903.6	2.18±0.05	
57119.29	1261.4	1.45±0.06	
57120.36	1578.7	1.26±0.04	
57121.06	1049.5	1.17±0.04	
Chandra MEG	57116.83	69008	0.0751±0.0010
Chandra HEG	57116.83	69008	0.1214±0.0013
NuSTAR FPMA	57116.12	42340	3.665±0.009
NuSTAR FPMB	57116.12	42340	3.626±0.009

**Notes.\*** Modified Julian Date. The count rates were measured in the following energy ranges: *Swift* XRT — 0.3–10.0 keV, *Chandra* MEG — 0.4–5.0 keV, *Chandra* HEG — 0.8–10.0 keV, *NuSTAR* FPM — 3–79 keV.

**Table 2.** The *Swift* UVOT magnitudes of GK Per obtained in quiescence.

MJD	Filter	Exp. (s)	Mag.
56115.284	UVW1	361	15.69±0.02
56115.279	UVM2	413	16.75±0.03
56115.274	UVW2	413	16.67±0.02
56117.086	UVW1	319	15.85±0.02
56117.082	UVM2	316	16.95±0.04
56117.078	UVW2	316	16.92±0.03
56118.014	UVW1	143	15.67±0.03
56118.013	UVM2	112	16.74±0.05
56118.012	UVW2	112	16.68±0.04

**Table 3.** The best-fitting model parameters of the *NuSTAR* mean + *Chandra* HETG, on-pulse and off-pulse *NuSTAR* FPMA spectra. The model is `constant×TBabs×pwab×(vmcflow + gaussian)`. The errors represent the 90% confidence region for a single parameter. We adopted FPMA Constant=1 and FPMB C.=1.089.

Component	Parameter	Value		
		Mean	On-pulse	Off-pulse
TBabs	nH ( $\times 10^{22}$ cm $^{-2}$ )	0.17	0.17	0.17
pwab	nH <sub>min</sub> ( $\times 10^{22}$ cm $^{-2}$ )	7.2 $^{+0.4}_{-0.4}$	7.4 $^{+1.1}_{-1.3}$	7.8 $^{+2}_{-2}$
	nH <sub>max</sub> ( $\times 10^{22}$ cm $^{-2}$ )	520 $^{+30}_{-30}$	550 $^{+40}_{-40}$	530 $^{+50}_{-50}$
	$\beta$	-0.199 $^{+0.016}_{-0.016}$	-0.26 $^{+0.05}_{-0.04}$	-0.16 $^{+0.07}_{-0.07}$
vmcflow	T <sub>low</sub> (keV)	0.0808	0.0808	0.0808
	T <sub>high</sub> (keV)	16.2 $^{+0.5}_{-0.4}$	16.2	16.2
	Fe	0.105 $^{+0.012}_{-0.012}$	0.105	0.105
	Ni	0.1	0.1	0.1
	$\dot{m}^a$	2.6 $^{+0.2}_{-0.2}$	3.69 $^{+0.12}_{-0.11}$	1.88 $^{+0.09}_{-0.05}$
Gaussian	E (keV)	6.40	6.40	6.40
	$\sigma$ (keV)	0.046 $^{+0.012}_{-0.008}$	0.046	0.046
	norm ( $\times 10^{-4}$ )	40 $^{+2}_{-2}$	50 $^{+5}_{-5}$	33 $^{+5}_{-4}$
	EW (eV)	210 $^{+30}_{-20}$	191 $^{+18}_{-19}$	250 $^{+130}_{-200}$
Flux	absorbed <sup>b</sup>	7.24 $^{+0.03}_{-3.07}$	10.15 $^{+0.05}_{-0.19}$	5.1 $^{+0.6}_{-0.6}$
Flux	unabsorbed <sup>b</sup>	24.2 $^{+1.0}_{-1.0}$	34.1 $^{+1.1}_{-1.0}$	17.5 $^{+0.8}_{-0.5}$
L ( $\times 10^{33}$ erg s $^{-1}$ )		63 $^{+3}_{-3}$	90 $^{+3}_{-3}$	46.1 $^{+2.1}_{-1.3}$
$\chi^2$		1.3		1.0

**Notes:** <sup>a</sup>mass accretion rate  $\times 10^{-8} M_{\odot}$  yr $^{-1}$ . <sup>b</sup>Absorbed and unabsorbed fluxes  $\times 10^{-10}$  ergs cm $^{-2}$  s $^{-1}$  in the 2.5–79 keV energy range. The unabsorbed flux was calculated with the `cflux` command in `xspec`. We assumed a 470 pc distance.

**Table 4.** Emission lines broadening, shifts and fluxes in the *Chandra* HETG spectra.

Line	E <sub>rest</sub> keV	E <sub>max</sub> keV	$\Delta v$ km s $^{-1}$	$\sigma$ km s $^{-1}$	F <sub>abs</sub> $\times 10^{-13}$ ergs cm $^{-2}$ s $^{-1}$	F <sub>unabs</sub> $\times 10^{-5}$ ph cm $^{-2}$ s $^{-1}$	F <sub>unabs</sub> $\times 10^{-13}$ ergs cm $^{-2}$ s $^{-1}$
Ne X	1.02195	1.017 $^{+0.004}_{-0.004}$	-1400 $^{+1200}_{-1200}$	2100 $^{+1000}_{-800}$	0.6 $^{+0.2}_{-0.2}$	5 $^{+2}_{-2}$	0.9 $^{+0.3}_{-0.4}$
Ne IX <sub>r</sub>	0.92200				0.5 $^{+0.3}_{-0.3}$	6 $^{+3}_{-3}$	0.8 $^{+0.5}_{-0.5}$
Ne IX <sub>i</sub>	0.91488			800 $^{+600}_{-300}$	0.6 $^{+0.3}_{-0.3}$	7 $^{+4}_{-4}$	1.0 $^{+0.5}_{-0.5}$
Ne IX <sub>f</sub>	0.90510				0.5 $^{+0.3}_{-0.3}$	6 $^{+4}_{-4}$	0.9 $^{+0.5}_{-0.5}$
Mg XII	1.47264	1.477 $^{+0.003}_{-0.002}$	900 $^{+600}_{-400}$	700 $^{+500}_{-300}$	0.2 $^{+0.1}_{-0.1}$	1.3 $^{+0.4}_{-0.4}$	0.3 $^{+0.1}_{-0.1}$
Mg XI <sub>r</sub>	1.35225				0.3 $^{+0.2}_{-0.2}$	0.8 $^{+0.9}_{-0.8}$	0.4 $^{+0.2}_{-0.2}$
Mg XI <sub>i</sub>	1.34332			1100 $^{+1800}_{-800}$	0.7 $^{+0.3}_{-0.2}$	4.9 $^{+2.3}_{-1.4}$	0.9 $^{+0.3}_{-0.3}$
Mg XI <sub>f</sub>	1.33121				0.16 $^{+0.12}_{-0.15}$	1.1 $^{+0.7}_{-0.6}$	0.20 $^{+0.15}_{-0.19}$
Si XIV	2.00608	2.008 $^{+0.002}_{-0.002}$	300 $^{+300}_{-300}$	800 $^{+400}_{-300}$	0.51 $^{+0.16}_{-0.15}$	1.7 $^{+0.5}_{-0.5}$	0.56 $^{+0.17}_{-0.17}$
Si XIII <sub>r</sub>	1.86500	1.8674 $^{+0.0029}_{-0.0015}$	400 $^{+300}_{-200}$		0.62 $^{+0.11}_{-0.25}$	1.9 $^{+0.8}_{-0.5}$	0.7 $^{+0.2}_{-0.2}$
Si XIII <sub>i</sub>	1.85423	1.8566 $^{+0.0029}_{-0.0015}$	400 $^{+500}_{-200}$	1000 $^{+1200}_{-700}$	0.34 $^{+0.2}_{-0.19}$	1.5 $^{+0.7}_{-0.8}$	0.4 $^{+0.2}_{-0.2}$
Si XIII <sub>f</sub>	1.83967	1.8421 $^{+0.0029}_{-0.0015}$	400 $^{+500}_{-200}$		0.77 $^{+0.16}_{-0.2}$	2.9 $^{+0.6}_{-0.8}$	0.8 $^{+0.2}_{-0.2}$
Fe XXVI	6.97316				8 $^{+4}_{-4}$	50 $^{+20}_{-20}$	50 $^{+20}_{-20}$
Fe XXV <sub>r</sub>	6.70040				6 $^{+4}_{-4}$	40 $^{+20}_{-20}$	40 $^{+30}_{-30}$
Fe XXV <sub>i</sub>	6.67000				5 $^{+4}_{-4}$	40 $^{+20}_{-20}$	40 $^{+30}_{-30}$
Fe XXV <sub>f</sub>	6.63659				6 $^{+3}_{-3}$	40 $^{+20}_{-20}$	40 $^{+20}_{-20}$
Fe K $_{\alpha}$	6.40384	6.400 $^{+0.007}_{-0.007}$	-200 $^{+300}_{-300}$	1600 $^{+300}_{-300}$	48 $^{+6}_{-6}$	350 $^{+50}_{-50}$	360 $^{+50}_{-50}$

**Notes:** We assumed that the value of  $\sigma$  is the same within a triplet for the Ne, Mg and Si lines. The distances between the lines in a triplet were fixed to the table values. The values of  $\sigma$  of the Fe XXVI and Fe XXV<sub>r,f,i</sub> lines were frozen to the instrumental spectral resolution. The absorbed and the unabsorbed fluxes in ergs cm $^{-2}$  s $^{-1}$  were calculated using the `cflux` command. The unabsorbed flux in ph cm $^{-2}$  s $^{-1}$  was calculated from the normalization constant of the Gaussian model.

**Table 5.** *R*, *G* and H-like/He-like<sub>r</sub> ratios.

Element	$R = f/i$	$G = (f + i)/r$	H-like/He-like <sub>r</sub>
Ne	0.9±0.7	2.4±1.7	1.1±0.8
Mg	0.2±0.2	2.8±1.6	0.8±0.5
Si	2.0±1.1	1.7±0.6	0.8±0.3
Fe	1.0±0.7	2.0±1.2	1.3±0.8

**Notes:** the values of *R* and *G* were calculated from the values of the unabsorbed flux from table 4.

**Table 6.** N VII emission line fluxes, measured in the *Chandra* MEG spectra of 2002 and 2015.

Observation	E max (keV)	central		red-shifted			blue-shifted		
		Flux*	Ph. flux**	E max	Flux	Ph. flux	E max	Flux	Ph. flux
2002 March 27	0.4998 <sup>+0.0003</sup> <sub>-0.0003</sub>	12±4	1.6±0.4	0.4977 <sup>+0.0006</sup> <sub>-0.0008</sub>	5±2	0.6±0.3			
2002 April 9	0.5000 <sup>+0.0003</sup> <sub>-0.0004</sub>	11±3	1.4±0.4	0.4973 <sup>+0.0005</sup> <sub>-0.0003</sub>	11±3	1.3±0.4	0.5026 <sup>+0.0002</sup> <sub>-0.0005</sub>	5±2	0.6±0.3
2015 April 4	0.50036	9±6	1.1±0.7	0.4980	17±8	1.2±1.0			

**Notes:** \*Unabsorbed flux  $\times 10^{-13}$  ergs  $\text{cm}^{-2}$   $\text{s}^{-1}$ . \*\*Unabsorbed photon flux  $\times 10^{-3}$  photons  $\text{cm}^{-2}$   $\text{s}^{-1}$ . The fluxes were measured from the Gaussian fits, shown in fig. 12 using `cflux` and `cpflux` commands. All the line widths were fixed to the value of the instrumental resolution. In these fits we assumed the same value of the interstellar absorption as in the rest of the paper:  $0.17 \times 10^{22} \text{cm}^{-2}$ .

**Table 7.** Model parameters used for the fit of *Chandra* MEG spectrum apart from that listed in the first column of table 3. The model is `TBabs × (pwab × (vmcflow + gaussian) + bb + gaussian)`. The fit was performed for two different temperatures. The parameters without errors were fixed to the values in this table. The Fe and Ni abundances were fixed to 0.105 and 0.1, respectively.

Component	Parameter	Value	
vapec	T (keV)	0.9	4.9 <sup>+1.4</sup> <sub>-0.8</sub>
	norm ( $\times 10^{-3}$ )	1.1 <sup>+0.1</sup> <sub>-0.1</sub>	2.6 <sup>+1.5</sup> <sub>-1.5</sub>
bb	T (eV)	66	66
	norm ( $\times 10^{-4}$ )	13 <sup>+2</sup> <sub>-2</sub>	12 <sup>+2</sup> <sub>-2</sub>
Gaussian	E (keV)	0.4988 <sup>+0.0011</sup> <sub>-0.0009</sub>	0.4988 <sup>+0.0011</sup> <sub>-0.0009</sub>
	$\sigma$ (keV)	0.0019 <sup>+0.0011</sup> <sub>-0.0009</sub>	0.0019 <sup>+0.0011</sup> <sub>-0.0009</sub>
	norm ( $\times 10^{-4}$ )	28 <sup>+13</sup> <sub>-12</sub>	29 <sup>+13</sup> <sub>-12</sub>

**Table 8.** The best fitting model parameters of the *Swift* XRT data.  $\text{TBabs} \times (\text{pwab} \times (\text{vmcflow} + \text{gaussian}) + \text{vapec} + \text{bb})$ . The Fe and Ni abundances of the *vmcflow* and *vapec* components were fixed to 0.106 and 0.1, respectively. The errors represent the 90% confidence region for a single parameter.

Component	Parameter	Value	
		first two weeks	second two weeks
TBabs	$n\text{H}^{a,b}$	0.17	0.17
pwab	$n\text{H}_{\text{min}}^b$	$2.7^{+0.6}_{-1.2}$	$5.0^{+1.1}_{-1.0}$
	$n\text{H}_{\text{max}}^b$	$75^{+18}_{-14}$	$90^{+20}_{-20}$
	$\beta^a$	0	0
vmcflow	$T_{\text{high}}$ (keV)	$17^{+10}_{-4}$	$17^{+15}_{-4}$
	$\dot{m}^c$	$0.7^{+0.5}_{-0.3}$	$0.6^{+0.3}_{-0.3}$
Gaussian	E (keV)	6.4	6.4
	$\sigma$ (keV)	0.04	0.04
	norm ( $\times 10^{-4}$ )	$6^{+2}_{-2}$	$15^{+2}_{-2}$
vapec	T (keV)	$>1.9$	$0.80^{+0.20}_{-0.10}$
	norm ( $\times 10^{-3}$ )	$2.5^{+3.1}_{-0.5}$	$3.7^{+0.3}_{-0.3}$
bb	T (eV)	$75^{+3}_{-3}$	$63^{+3}_{-2}$
	norm ( $\times 10^{-4}$ )	$6.2^{+1.0}_{-0.8}$	$36^{+5}_{-5}$
Flux $_{0.3-2\text{keV}}^d$	abs.	$4.6^{+0.3}_{-1.0}$	$11.9^{+0.2}_{-0.5}$
	unabs.	420	430
Flux $_{2-10\text{keV}}^d$	abs.	$165^{+2}_{-60}$	$117^{+2}_{-50}$
	unabs.	507	451
$L_{\text{bb}}$ ( $\times 10^{33}\text{erg s}^{-1}$ )		$1.33^{+0.20}_{-0.17}$	$8.6^{+0.7}_{-0.7}$
$R_{\text{bb}}^g$ ( $\times 10^6\text{cm}$ )		$1.70^{+0.13}_{-0.12}$	$5.3^{+0.5}_{-0.3}$
$L_{2-10\text{keV}}$ ( $\times 10^{33}\text{erg s}^{-1}$ )		13.4	11.9
$\chi^2$		1.7	

**Notes:** <sup>a</sup>Frozen parameter. <sup>b</sup> $\times 10^{22}\text{ cm}^{-2}$ .

<sup>c</sup>Mass accretion rate  $\times 10^{-8}M_{\odot}\text{ yr}^{-1}$ . <sup>d</sup> $\times 10^{-12}\text{erg cm}^{-2}\text{ s}^{-1}$ .

<sup>g</sup> Radius of the emitting region. We assumed a 470 pc distance.